

Strong magnetic correlations to 900 K in single crystals of the trigonal antiferromagnetic insulators SrMn_2As_2 and CaMn_2As_2

N. S. Sangeetha, Abhishek Pandey,* Zackery A. Benson, and D. C. Johnston†

Ames Laboratory and Department of Physics and Astronomy, Iowa State University, Ames, Iowa 50011, USA

(Dated: June 13, 2016)

Crystallographic, electronic transport, thermal and magnetic properties are reported for SrMn_2As_2 and CaMn_2As_2 single crystals grown using Sn flux. Rietveld refinements of powder x-ray diffraction data show that the two compounds are isostructural and crystallize in the trigonal CaAl_2Si_2 -type structure (space group $P\bar{3}m1$), in agreement with the literature. Electrical resistivity ρ versus temperature T measurements demonstrate insulating ground states for both compounds with activation energies of 85 meV for SrMn_2As_2 and 61 meV for CaMn_2As_2 . In a local-moment picture, the $\text{Mn}^{+2} 3d^5$ ions are expected to have high-spin $S = 5/2$ with spectroscopic splitting factor $g \approx 2$. Magnetic susceptibility χ and heat capacity measurements versus T reveal antiferromagnetic (AFM) transitions at $T_N = 120(2)$ K and $62(3)$ K for SrMn_2As_2 and CaMn_2As_2 , respectively. The anisotropic $\chi(T \leq T_N)$ data indicate that the hexagonal c axis is the hard axis and hence that the ordered Mn moments are aligned in the ab plane. The $\chi(T)$ data for both compounds and the $C_p(T)$ for SrMn_2As_2 show strong dynamic short-range AFM correlations from T_N up to at least 900 K, likely associated with quasi-two-dimensional connectivity of strong AFM exchange interactions between the Mn spins within the corrugated honeycomb Mn layers parallel to the ab plane.

PACS numbers: 75.50.Ee, 74.70.Xa, 75.40.-s, 72.15.Eb

I. INTRODUCTION

The body-centered tetragonal AM_2X_2 ternary compounds (A = rare or alkaline earth, M = transition metal, X = Si, Ge, P, As, Sb) with the ThCr_2Si_2 structure¹ have generated tremendous interest in the scientific community due to their novel electronic and magnetic properties. Prominent among these is the iron-arsenide family of parent compounds AFe_2As_2 (A = Ca, Sr, Ba, Eu).^{2–10} These materials are metallic and show nearly contiguous antiferromagnetic (AFM) spin-density wave and structural transitions at temperatures T up to ~ 200 K. The suppression of these transitions by external pressure or chemical doping leads to superconductivity with bulk superconducting transition temperatures T_c up to 56 K. It is believed that the FeAs layer as the conducting sheet in this structure plays a crucial role in the occurrence of superconductivity.^{2–10} Hence, it is important to investigate other related materials with similar compositions and structures in the search for new superconductors and other novel phenomena. For example, SrNi_2As_2 ($T_c = 0.62$ K, Ref. 11) and BaNi_2As_2 ($T_c = 0.7$ K, Ref. 12) were both found to be superconductors.

On the other hand, SrCo_2As_2 (Refs. 13–15) and BaCo_2As_2 (Refs. 16,17) are correlated metals with no structural, superconducting or long-range magnetic ordering transitions. From inelastic neutron scattering measurements, SrCo_2As_2 is found to exhibit strong AFM correlations at the same stripe wavevector as do the superconducting iron arsenides, which raises the interesting question of why SrCo_2As_2 is not a high- T_c superconductor.¹⁴ The reason has been suggested from NMR measurements to be that SrCo_2As_2 exhibits strong *ferromagnetic* (FM) spin correlations/fluctuations in ad-

dition to the AFM correlations and these compete with the AFM correlations that are the presumptive glue for superconductivity in these systems. Subsequent NMR studies indicated that the large range of T_c observed within the FeAs-based systems may also arise from the competition between FM and AFM correlations.¹⁸

Recently significant attention has focussed on Mn arsenides. Our studies of the properties of the parent and doped BaMn_2As_2 systems were originally motivated by their potential to be ThCr_2Si_2 -type high- T_c superconductors analogous to the cuprates. The semiconductor BaMn_2As_2 shows G-type (checkerboard-type) local-moment collinear AFM order below its high Néel temperature $T_N = 625$ K with the ordered moments aligned along the tetragonal c axis.^{19–21} Thus magnetoelastic coupling does not cause a distortion of the crystal structure below T_N , contrary to the orthorhombic distortion associated with AFM ordering in the AFe_2As_2 compounds due to the collinear Fe ordered moments aligned in the ab plane. An optical gap of 48 meV was inferred for BaMn_2As_2 from the optical conductivity,²² consistent with results from the electrical resistivity ρ versus temperature T measurements in the ab plane.¹⁹ Furthermore, this optical study²² found that BaMn_2As_2 is much more two-dimensional in its electronic properties than are the AFe_2As_2 parent compounds.¹⁹ A neutron scattering study of isostructural BaMn_2Bi_2 found the same G-type AFM structure as in BaMn_2As_2 but with a lower $T_N = 387$ K.²³

Only 1.6% K substitution for Ba transforms BaMn_2As_2 into a local-moment AFM metal.^{24,25} Higher doping levels lead to the onset of FM at $\approx 16\%$ K-doping²⁶ and half-metal FM behavior below the Curie temperature $T_C \sim 100$ K at 40% K doping (Refs. 27,28) and at 60%

Rb doping.²⁹ The FM is thus thought to be associated with FM ordering of the itinerant doped-hole spins and coexists with the G-type AFM order of the local Mn moments with $T_N > 300$ K.^{28,30}

Unlike BaMn_2As_2 with the tetragonal ThCr_2Si_2 structure, the compounds SrMn_2As_2 and CaMn_2As_2 both crystallize in the trigonal CaAl_2Si_2 -type structure^{31,32} containing a corrugated honeycomb Mn sublattice which can be viewed as a triangular lattice bilayer. The possibility of geometrically-frustrated triangular-lattice exchange connectivity exists and such compounds often show novel physical behaviors associated with the geometric frustration.^{33–35} Single crystals of SrMn_2As_2 were grown previously using Sn flux.³⁶ These authors' in-plane electrical resistivity $\rho(T)$ measurements indicated that the ground state is insulating with activation energies of 0.29–0.64 eV depending on the T range, and their magnetic susceptibility $\chi(T)$ measurements indicated an AFM transition at $T_N = 125$ K.³⁶

Two neutron powder diffraction studies^{37,38} of the related CaAl_2Si_2 -type CaMn_2Sb_2 revealed AFM ordering below $T_N = 88$ K and 85 K, respectively, with an AFM propagation vector $\mathbf{k} = (0, 0, 0)$, i.e., the crystal and AFM unit cells are the same. In the former paper the AFM structure was deduced to be collinear, with the ordered moments aligned in the ab plane with a low- T ordered moment of $2.8(1) \mu_B/\text{Mn}$, where μ_B is the Bohr magneton. In the latter paper, a model was favored with the ordered moments canted at $\pm 25^\circ$ with respect to the ab plane with an ordered moment of $3.38(6) \mu_B/\text{Mn}$.

Herein, we report the growth, crystal structure, $\rho(T)$, magnetization as a function of magnetic field $M(H)$, $\chi(T)$ and heat capacity $C_p(T)$ measurements of CaMn_2As_2 and SrMn_2As_2 single crystals. These studies were initiated because of the above-noted possibility that the Mn spin lattice might exhibit novel magnetic behaviors associated with the presence of geometric frustration within the triangular-lattice Mn layers. If the strongest AFM interactions are indeed within a triangular lattice layer, this should lead to a noncollinear AFM structure below T_N . Instead, in a companion neutron diffraction study to the present work, the AFM structure of SrMn_2As_2 was found to be collinear with the ordered Mn moments aligned in the ab plane with magnitude $3.6 \mu_B/\text{Mn}$.³⁹ This magnetic structure is the same as one of the two AFM structures proposed for CaMn_2Sb_2 (Ref. 37) discussed above.

We discovered that the $\chi(T)$ of SrMn_2As_2 and CaMn_2As_2 and the $C_p(T)$ of SrMn_2As_2 above their respective Néel temperatures T_N of 120 and 62 K exhibit behaviors characteristic of strong dynamic short-range AFM spin correlations up to at least 900 K, likely arising from quasi-two-dimensional connectivity of strong AFM Mn–Mn exchange interactions within the corrugated honeycomb Mn spin sublattice. This result is interesting because such strong AFM spin correlations up to high temperatures and the suppression of T_N to much lower temperatures than expected from molecular field theory,

due to AFM fluctuations associated with the low dimensionality of the exchange interaction connectivity, may give rise to novel physical properties upon doping the compounds into the metallic state.

II. EXPERIMENTAL DETAILS

Single crystals of SrMn_2As_2 and CaMn_2As_2 were grown using Sn flux. High-purity elements Sr (99.95%) from Sigma Aldrich, and Ca (99.95%), Co (99.998%), As (99.9999%) and Sn (99.999%) from Alfa Aesar were taken in the ratio (Sr,Ca):Mn:As:Sn = 1:2:2:20 and placed in an alumina crucible that was subsequently placed in a silica tube that was evacuated, partially refilled with high-purity argon ($\approx 1/4$ atm pressure) and then sealed. After preheating at 600°C for 5 h, the assembly was heated to 1150°C at the rate of 50°C/h and held at this temperature for 20 h for homogenization. Then the furnace was slowly cooled at the rate of 5°C/h to 700°C . At this temperature the molten Sn flux was decanted using a centrifuge. Shiny hexagonal-shape single crystals of maximum dimensions $4 \times 3 \times 1 \text{ mm}^3$ were obtained.

Semiquantitative chemical analyses of the single crystals were performed using a JEOL scanning electron microscope (SEM) equipped with an EDX (energy-dispersive x-ray analysis) detector, where a counting time of 120 s was used. A room-temperature powder x-ray diffraction (XRD) pattern was recorded on crushed single crystals using a Rigaku Geigerflex powder diffractometer with Cu $K\alpha$ radiation at diffraction angles 2θ from 10° to 110° with a 0.02° step width. The data were analysed by Rietveld refinement using FullProf software.⁴⁰

$M(T)$ measurements for $1.8 \text{ K} \leq T \leq 300 \text{ K}$ and $M(H)$ measurements for $H \leq 5.5 \text{ T}$ were carried out using a Quantum Design, Inc., Magnetic Properties Measurement System (MPMS). The high-temperature $M(T)$ for $300 \text{ K} \leq T \leq 900 \text{ K}$ was measured using the vibrating sample magnetometer (VSM) option of a Quantum Design, Inc., Physical Properties Measurement System (PPMS). In this paper we exclusively use Gaussian cgs units for M , χ and H (see Sec. 3.5.1 of Ref. 2). In this system of units, the Tesla (T) is a unit of convenience for H defined as $1 \text{ T} = 10^4 \text{ Oe}$, where Oe is the conventional cgs unit for H .

$C_p(T)$ data were obtained using a relaxation method with the heat capacity option of the PPMS. Four-probe $\rho(T)$ data were obtained with an ac current amplitude $I = 1 \mu\text{A}$ at a frequency of 37.7 Hz using the ac transport option of the PPMS. Electrical contacts to a crystal were made by soldering 0.05 mm diameter Pt wire to a crystal using indium solder.

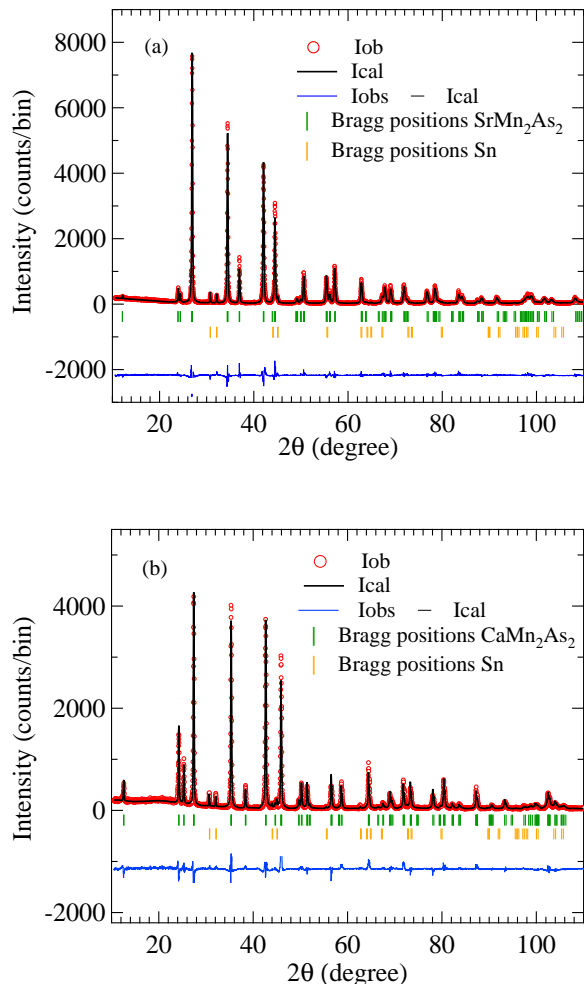


FIG. 1: (Colour online) Powder x-ray diffraction patterns (open circles) of (a) SrMn_2As_2 and (b) CaMn_2As_2 at room temperature. The solid line represents the Rietveld refinement fit calculated for the CaAl_2Si_2 -type trigonal structure with space group $P\bar{3}m1$ together with the Sn impurity phase.

III. EXPERIMENTAL RESULTS

A. Crystal Structure

The crystal symmetry of several SrMn_2As_2 and CaMn_2As_2 crystals was checked by x-ray Laue back scattering which showed trigonal symmetry with well-defined diffraction spots which clearly indicated the good quality of the crystals. In this paper we use the hexagonal setting for the trigonal unit cell. The data also revealed that the SrMn_2As_2 and CaMn_2As_2 platelike crystals grow with the plate surface parallel to the hexagonal ab plane. SEM imaging and EDX analyses were performed to check the chemical composition and surface morphology of the crystals. The average elemental ratio of the samples was in agreement with the expected 1:2:2

TABLE I: Crystallographic and Rietveld refinement parameters obtained from powder XRD of SrMn_2As_2 and CaMn_2As_2 crystals. The structures are trigonal CaAl_2Si_2 -type with space group $P\bar{3}m1$. The atomic coordinates of SrMn_2As_2 and CaMn_2As_2 are Sr/Ca: $1a$ (0, 0, 0); Mn: $2d$ ($1/3$, $2/3$, z_{Mn}); and As: $2d$ ($1/3$, $2/3$, z_{As}). The shortest Mn–Mn interatomic distances in SrMn_2As_2 and CaMn_2As_2 [see Fig. 2(b)] are also listed.

	SrMn_2As_2	CaMn_2As_2
Lattice parameters		
a (Å)	4.2962(1)	4.2376(1)
c (Å)	7.2997(2)	7.0331(2)
c/a	1.6991(1)	1.6596(1)
V_{cell} (Å ³)	116.682(6)	109.372(6)
Atomic coordinates		
z_{Mn}	0.6231(1)	0.6248(4)
z_{As}	0.2667(2)	0.2537(3)
Refinement quality		
χ^2	3.05	4.03
R_p (%)	10.3	12.7
R_{wp} (%)	13.6	16.4
Shortest Mn–Mn distances (Å)		
d_1	3.06306(8)	3.0112(2)
d_2	4.29620(5)	4.23760(5)
d_3	5.27633(7)	5.1985(2)
d_{z1}	6.0357(2)	5.8171(4)
d_{z2}	7.2997(2)	7.0331(2)

stoichiometry of the compounds to within the errors. The amount of Sn incorporated into the crystal structure from the Sn flux is zero to within the experimental error. The present analyses did not show any other elements.

The phase purity of our SrMn_2As_2 and CaMn_2As_2 crystals was confirmed by powder XRD. Their XRD patterns at 300 K along with the results of Rietveld refinements are shown in Figs. 1(a) and 1(b), respectively. One sees the presence of adventitious elemental Sn flux, so two-phase Rietveld refinements were carried out. The refinement results confirm that the crystals have the trigonal CaAl_2Si_2 -type structure with space group $P\bar{3}m1$. The refinement and crystal parameters obtained are listed in Table I. The crystal parameters are in good agreement with previously reported values.^{31,32,36}

Figure 2(a) shows a unit cell of trigonal SrMn_2As_2 and CaMn_2As_2 in the hexagonal setting. As shown in Figs. 2(b) and 2(d), the structure consists of corrugated honeycomb $[\text{Mn}_2\text{As}_2]^{-2}$ layers that are stacked along the c axis and separated by Sr^{+2} or Ca^{+2} cations, respectively. Alternatively, the Mn sublattice can be viewed as triangular double layers of Mn stacked along the c axis and separated by Ca or Sr atoms. The three smallest Mn–Mn interatomic distances [see Fig. 2(b)] are within the corrugated Mn honeycomb layers and are listed in

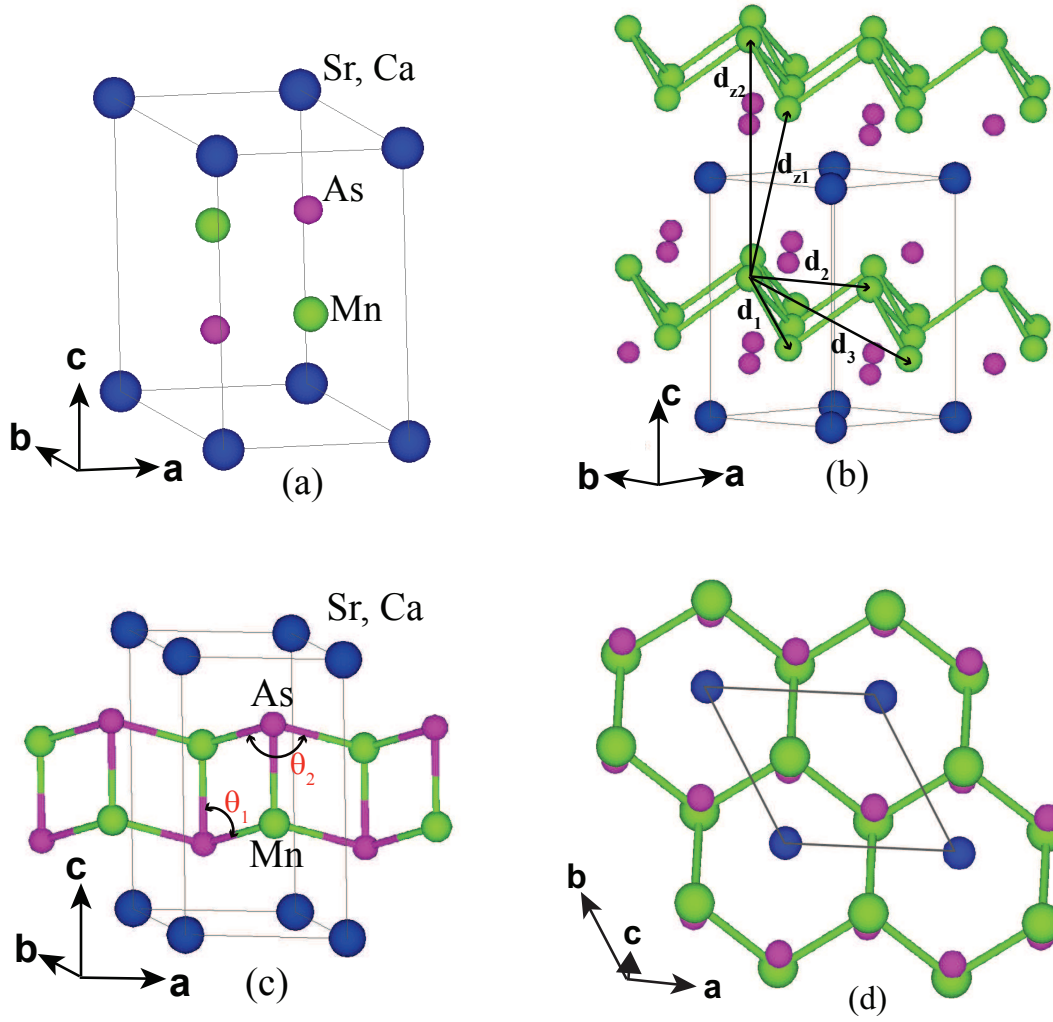


FIG. 2: (Colour online) Trigonal CaAl_2Si_2 -type crystal structure of SrMn_2As_2 and CaMn_2As_2 in the hexagonal setting. (a) Outline of a unit cell containing one formula unit. (b) Corrugated Mn honeycomb layers as viewed from nearly perpendicular to the c axis. The smallest Mn–Mn interatomic distances within a corrugated Mn honeycomb layer (d_1 , d_2 , d_3) and between layers (d_{z1} , d_{z2}) are indicated. (c) Expanded view of the structure from a view nearly perpendicular to the c axis showing the corrugated $[\text{Mn}_2\text{As}_2]^{-2}$ honeycomb layers separated by Sr or Ca. (d) Projection of the Mn sublattice onto the ab plane with a slight c axis component illustrating the corrugated Mn honeycomb lattice. The corrugated honeycomb lattice layer can be viewed as a triangular lattice bilayer [compare with panel (b)]. The outline of a unit cell in the ab plane is also shown.

Table I. The nearest-neighbor Mn–Mn distance (d_1) is between the two Mn atoms at different heights (z values) within a unit cell. The second-nearest-neighbor Mn–Mn distance (d_2) is between Mn atoms at the same height in adjacent unit cells along the ab plane forming a triangular-lattice layer, and the third-nearest-neighbor Mn–Mn distance (d_3) is between nearest-neighbor Mn atoms in adjacent unit cells in the ab plane. The nearest- and second-nearest-neighbor distances d_{z1} and d_{z2} between Mn atoms in adjacent layers in different unit cells along the c axis are also listed in Table I.

Since the minimum intralayer Mn–Mn distance $d_1 \approx 3 \text{ \AA}$ is much shorter than the minimum interlayer Mn–Mn distance ($d_{z1} \approx 6 \text{ \AA}$), CaMn_2As_2 and SrMn_2As_2 likely have a quasi-two-dimensional Mn–Mn exchange interac-

tion connectivity. This large spatial anisotropy in the exchange interactions should be obvious from $\chi(T > T_N)$ measurements, which is confirmed below. These exchange interactions could arise from direct Mn–Mn interactions and/or from indirect Mn–As–Mn superexchange interactions. The latter would likely occur via two main paths: (i) between first-nearest-neighbor Mn spins with $\angle \text{Mn-As-Mn}$ (θ_1) = 72° and another between second-nearest-neighbor Mn spins with $\angle \text{Mn-As-Mn}$ (θ_2) = 111° [see Fig. 2(c)]. It will be interesting to see which of these interactions are dominant within the unusual trigonal symmetry of the Mn spin lattice.

To summarize, the SrMn_2As_2 and CaMn_2As_2 trigonal structure is quite different from the body-centered tetragonal ThCr_2Si_2 structure found for the AFe_2As_2 parent

compounds that is composed of metal-arsenide tetrahedra separated by alkaline earth layers. The primary difference between them is the geometry of the transition metal layers. In SrMn_2As_2 and CaMn_2As_2 , the Mn bilayer is a corrugated Mn honeycomb lattice where each Mn atom is coordinated by three other Mn atoms at $\sim 90^\circ$ like the corner of the cube as seen in Figs. 2(b) and 2(c), whereas in ThCr_2Si_2 -type compounds such as BaMn_2As_2 or BaFe_2As_2 , the Mn or Fe network is a simple square-planar lattice where each Mn or Fe is coordinated by four other Mn or Fe atoms, also at 90° angles between them. On the other hand, the AFM in BaMn_2As_2 is quasi-two-dimensional,²¹ just as we find it to be in SrMn_2As_2 and CaMn_2As_2 from the $\chi(T)$ data in Sec. III C below.

B. In-Plane Electrical Resistivity

Figures 3(a) and 3(b) show $\rho(T)$ of SrMn_2As_2 and CaMn_2As_2 , respectively, from ~ 50 to 300 K measured in the ab plane. The data show that both compounds are semiconductors with insulating intrinsic ground states. We fitted $\rho(T)$ in the temperature region between 70 and 120 K by the expression $\log_{10} \rho = A + 2.303\Delta/k_B T$, where A is a constant, k_B is Boltzmann's constant and Δ is the activation energy. The fits are shown as the solid straight lines through the data in the insets of Figs. 3(a) and 3(b), which give the activation energies $\Delta = 85$ meV for SrMn_2As_2 and $\Delta = 61$ meV for CaMn_2As_2 . These activation energies are of the same order as previously obtained from $\rho(T)$ data for BaMn_2As_2 .¹⁹ Our activation energy for SrMn_2As_2 is significantly smaller than the previously reported values $\Delta = 0.29$ and 0.64 eV, depending on the T range, that were also obtained from single-crystal in-plane $\rho(T)$ data.³⁶

C. Magnetization and Magnetic Susceptibility

The zero-field-cooled (ZFC) magnetic susceptibility $\chi \equiv M/H$ versus T measured in $H = 0.1$ T and $H = 3$ T applied in the ab plane ($H \parallel ab$, χ_{ab}) and along the c axis ($H \parallel c$, χ_c) for single crystals of SrMn_2As_2 and CaMn_2As_2 are shown in Figs. 4 and 5, respectively.

Clear AFM transitions are observed in $\chi(T)$ at $T_N \approx 120$ K for SrMn_2As_2 and $T_N \approx 65$ K for CaMn_2As_2 , as indicated by vertical arrows in Figs. 4(a) and 5(a), respectively. We also performed FC (field-cooled) and ZFC $\chi(T)$ measurements at $H = 0.1$ T and $H = 3$ T (not shown here). No hysteresis was observed between the ZFC and FC data, which is consistent with long-range AFM ordering of SrMn_2As_2 and CaMn_2As_2 below their respective Néel temperatures. The data in Figs. 4(a) and 5(a) for $T > T_N$ are nearly isotropic, as expected for Mn^{+2} with spin $S = 5/2$ and $g \approx 2$.

From Figs. 4(a) and 5(a), the anisotropy in χ at $T < T_N$ indicates that the hard axis is the c axis and

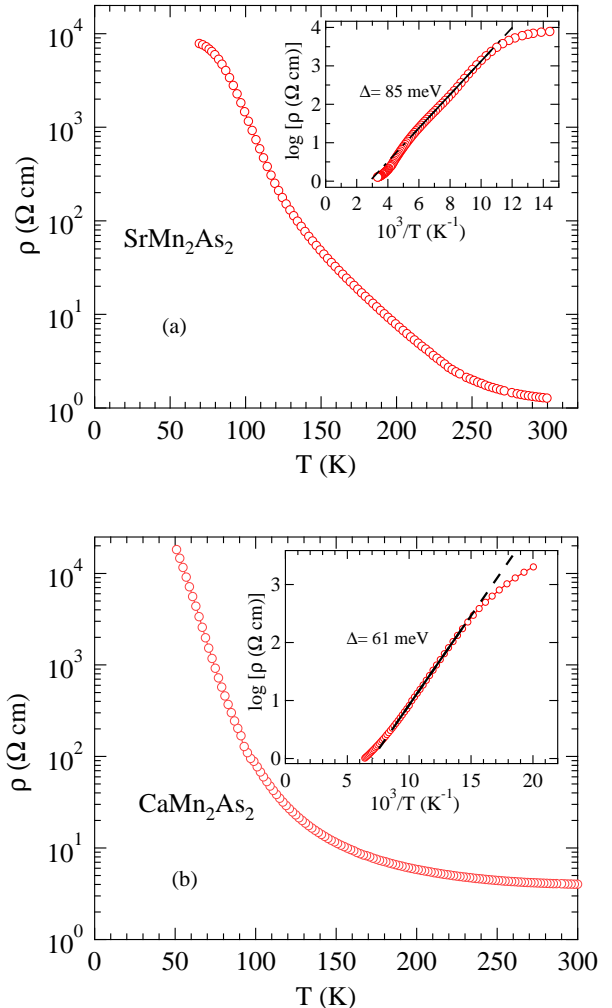


FIG. 3: (Colour online) In-plane electrical resistivity ρ of (a) SrMn_2As_2 and (b) CaMn_2As_2 versus temperature T from ~ 50 to 300 K. The insets show plots of $\log_{10} \rho$ versus $1000/T$. The solid straight lines through the data are fits over the temperature interval between 70 and 120 K by the expression $\log_{10} \rho = A + 2.303\Delta/T$ and the resulting fitted activation energies are listed. The dashed lines are extrapolations.

the ab plane is the easy plane for both compounds. Furthermore, the nonzero limits of $\chi_{ab}(T \rightarrow 0)$ suggest that the AFM structure could be either a collinear AFM with multiple domains aligned within the ab plane or an intrinsic noncollinear structure with moments again aligned in the ab plane.^{41–44} For collinear ordering, magnetic dipole interactions between the Mn moments favor ab -plane moment alignment over c -axis alignment.⁴⁵ In SrMn_2As_2 [see Fig. 4(b)], the anisotropy in χ for $T < T_N$ is eliminated by a field of 3 T, which indicates a relatively small magnetocrystalline anisotropy compared to that in CaMn_2As_2 judging from Fig. 5(b). The small upturns in χ in Figs. 4 and 5 below ~ 20 K are believed due to trace amounts of paramagnetic local-moment impurities.

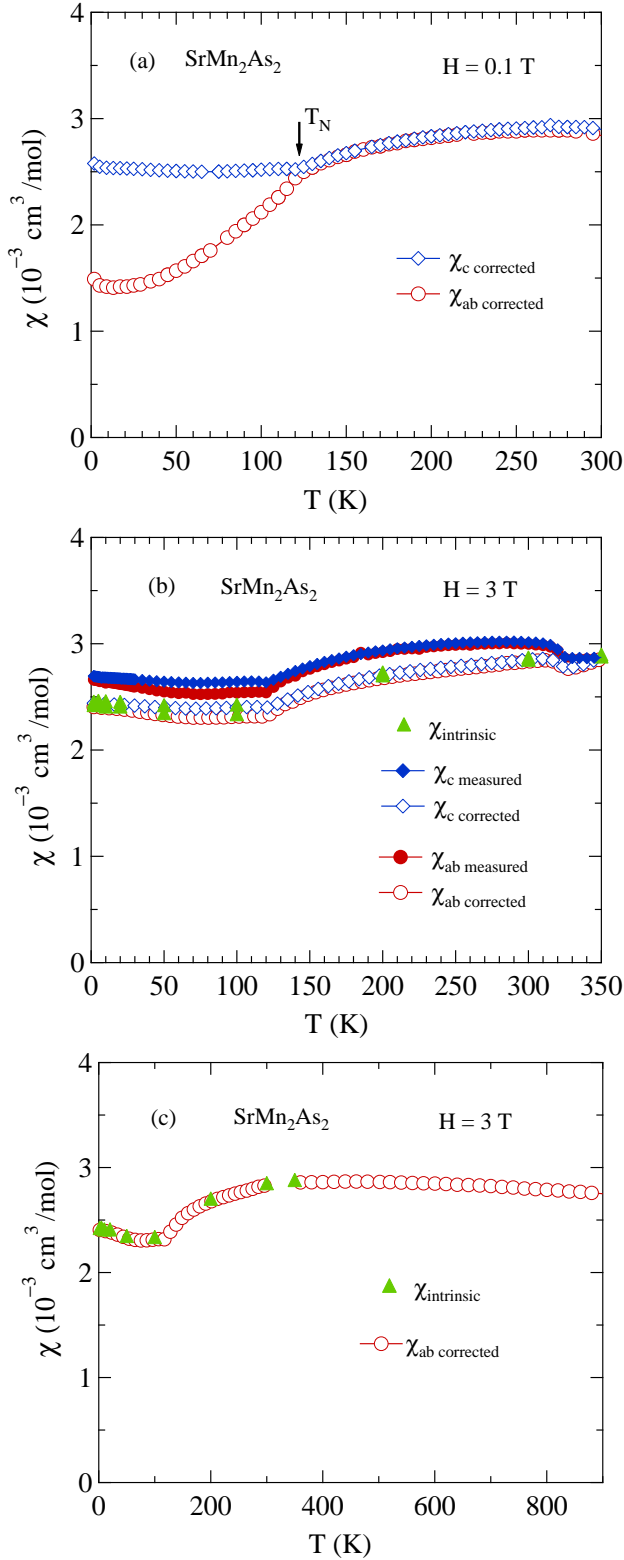


FIG. 4: (Color online) ZFC magnetic susceptibility $\chi(T)$ of SrMn_2As_2 from 1.8 to 300 K measured in magnetic fields (a) $H = 0.1 \text{ T}$ and (b) $H = 3 \text{ T}$ applied in the ab plane ($H \parallel ab$, χ_{ab}) and along the c axis ($H \parallel c$, χ_c). (c) ZFC susceptibility versus T for $1.8 \leq T \leq 900 \text{ K}$ measured in $H = 3 \text{ T}$ applied in the ab plane ($H \perp c$). The “intrinsic” values are obtained from $M(H)$ isotherms using Eq. (1) and the “corrected” ones are obtained from $M(T)$ data using Eq. (2).

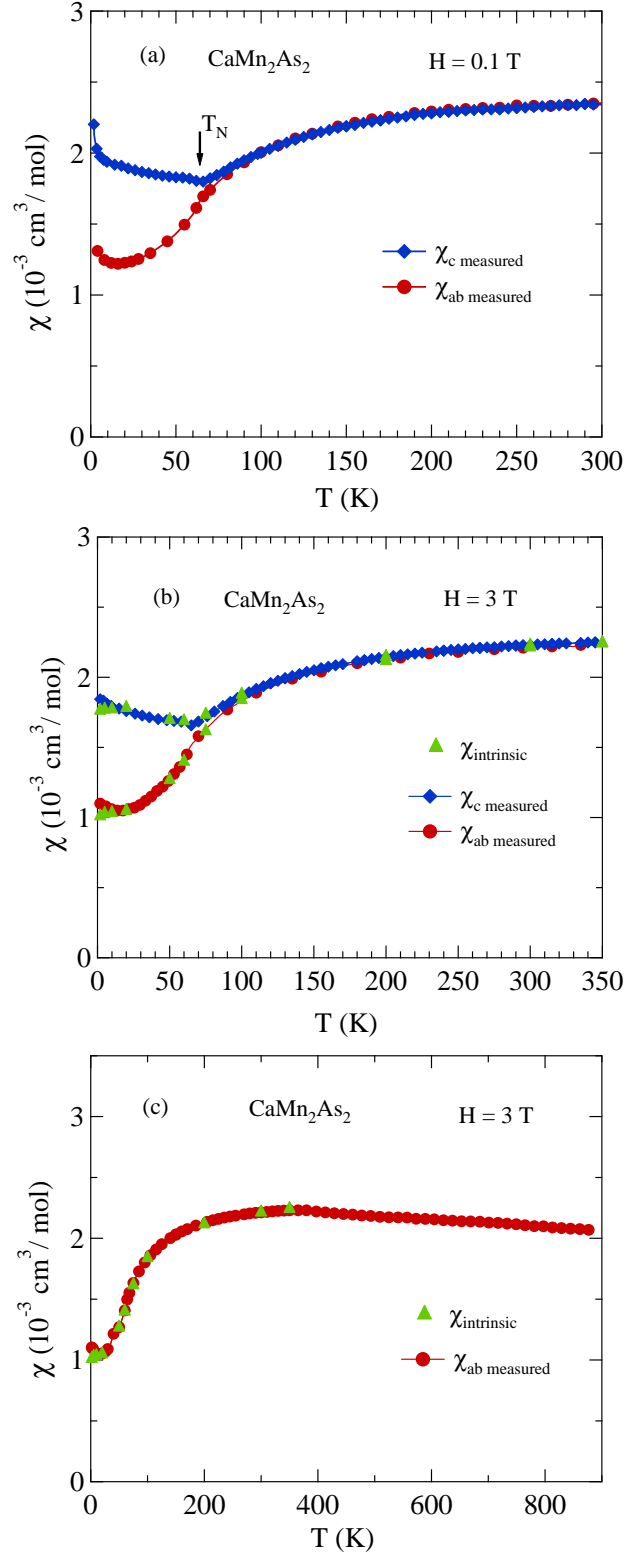


FIG. 5: (Color online) Magnetic susceptibility data for CaMn_2As_2 . The plot and symbol designations are the same as for SrMn_2As_2 in Fig. 4.

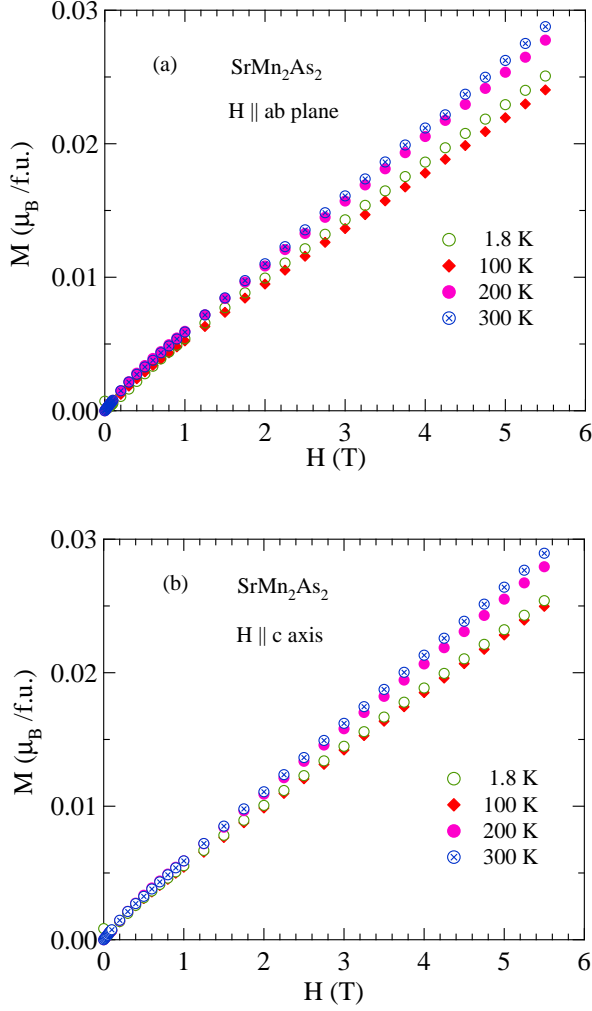


FIG. 6: (Color online) Magnetization M versus magnetic field H at various temperatures T with (a) H in the ab plane ($H \parallel ab$) and with (b) H along the c axis ($H \parallel c$) for SrMn_2As_2 .

A small jump in $\chi(T)$ is observed for SrMn_2As_2 in Fig. 4(b) on cooling below about 320 K. This is believed due to FM MnAs impurities with this Curie temperature that are present on the crystal surface and/or as an inclusion in the crystal, as previously observed for BaMn_2As_2 crystals.¹⁹ To extract the intrinsic magnetic behavior of SrMn_2As_2 , we carried out $M(H)$ isotherm measurements at various temperatures. Figures 6 and 7 show isothermal $M(H)$ data for SrMn_2As_2 and CaMn_2As_2 crystals, respectively, at different T for $H \parallel ab$ plane (M_{ab}) and $H \parallel c$ axis (M_c). The $M(H)$ curves are almost linear at high fields, but for SrMn_2As_2 one sees nonlinearities at low fields ($H < 1\text{--}2$ T) for $T < 200$ K, confirming the presence of saturable FM impurities.

To extract the intrinsic χ (χ_{int}) we fitted the $M(H)$ data in the high-field range $H = 3.5\text{--}5.5$ T by the linear

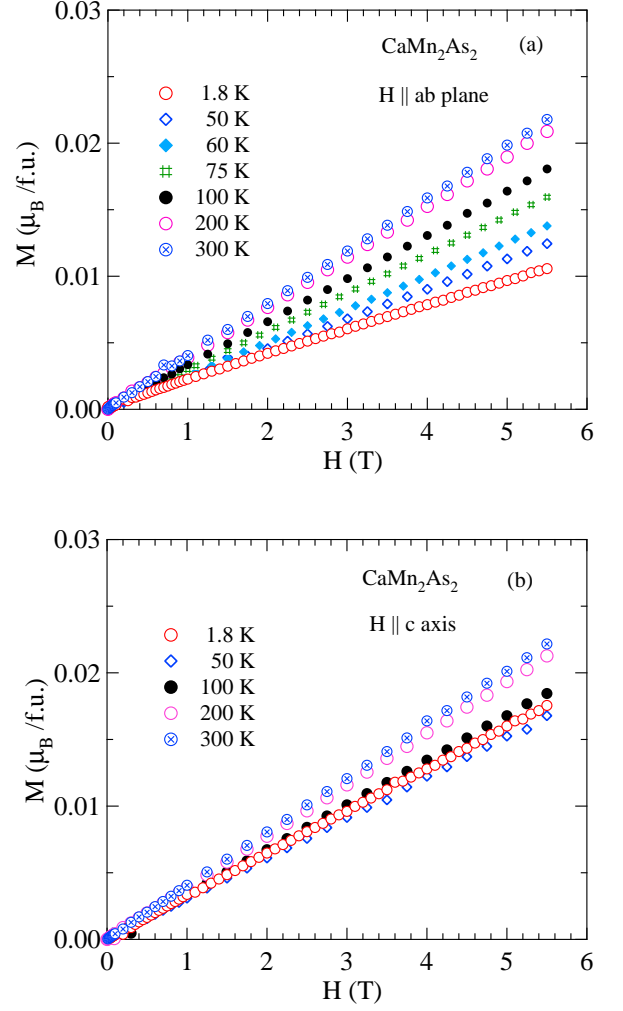


FIG. 7: (Color online) Magnetization M versus magnetic field H at various temperatures T with (a) H in the ab plane ($H \parallel ab$) and with (b) H along the c axis ($H \parallel c$) for CaMn_2As_2 .

relation

$$M(H, T) = M_s(T) + \chi_{\text{int}}(T)H, \quad (1)$$

where $M_s(T)$ is the saturation magnetization due to the FM impurities. The $T \rightarrow 0$ value of M_s for SrMn_2As_2 is $7 \text{ G cm}^3/\text{mol} = 0.0013 \mu_B/\text{f.u.}$, which corresponds to 0.04 mol% of MnAs impurities using the saturation moment of $\approx 3.5 \mu_B/\text{f.u.}$ (Refs. 46,47) for MnAs. The $\chi(T) \equiv M(T)/H$ data in Figs. 4(b) and 5(b) were measured with $H = 3$ T. Therefore, we obtained the intrinsic χ from the isotherm data according to

$$\chi_{\text{int}}(T) = \frac{M_{\text{measured}}(T) - M_s(T)}{3 \text{ T}}. \quad (2)$$

The $\chi_{\text{int}}(T)$ data are shown by the filled green triangles in Figs. 4(b) and 5(b). It is seen that the $\chi_{\text{int}}(T)$ data for CaMn_2As_2 match very well for both field directions

with the $\chi \equiv M/H$ data in Fig. 5(b), indicating a clean crystal without any detectable FM impurities.

In order to further clarify the magnetism in these systems we measured $\chi(T) \equiv M(T)/H$ in the extended temperature range up to 900 K for SrMn_2As_2 and CaMn_2As_2 as shown in Figs. 4(c) and 5(c), respectively. One sees that χ exhibits very broad maxima at ~ 400 K for both compounds. This feature is a signature of a low-dimensional local-moment AFM system.²¹ Thus SrMn_2As_2 and CaMn_2As_2 undergo a phase transition to a long-range ordered state below T_N , preceded by strong short-range AFM order at higher temperatures. Indeed, the Curie-Weiss temperature region of χ is not reached even at 900 K, indicating that strong AFM correlations survive to significantly higher temperatures.

From the Mn–Mn interatomic distances discussed in Sec. III A, we inferred that the Mn–Mn exchange coupling along the c axis between the corrugated honeycomb Mn layers in the ab plane is much smaller than within the layers. We confirm this here and in addition infer that the Mn–Mn exchange coupling within the corrugated honeycomb layers is dominantly antiferromagnetic.

D. Heat Capacity

Figures 8(a) and 8(b) show zero-field $C_p(T)$ data for SrMn_2As_2 and CaMn_2As_2 , respectively. The sharp anomalies in $C_p(T)$ at 120(2) K in SrMn_2As_2 and at 62(3) K in CaMn_2As_2 are the respective Néel temperatures of the two compounds, which are in good agreement with T_N values found above from the respective $\chi(T)$ data.

1. Low-Temperature Behaviors

The insets of Figs. 8(a) and 8(b) show $C_p(T)/T$ versus T^2 between 1.8 and 5 K. At low temperatures we model the $C_p(T)$ data by⁴⁸

$$C_p = \gamma T + \beta T^3, \quad (3)$$

where the coefficient γ is usually due to the electronic contribution (Sommerfeld coefficient) and β is the coefficient of the Debye T^3 lattice contribution in the absence of three-dimensional AFM spin-wave contributions. The data were therefore fitted by the expression

$$\frac{C_p}{T} = \gamma + \beta T^2, \quad (4)$$

From the fits of Eq. (6) to the data in the insets of Figs. 8(a) and 8(b) we obtain $\gamma = 0.0(1)$ mJ/(mol K²) for SrMn_2As_2 and $0.05(7)$ mJ/(mol K²) for CaMn_2As_2 . The null values of γ are consistent with the insulating ground states found from the $\rho(T)$ measurements in Sec. III B.

The fitted values for β are

$$\beta = 0.35(1) \frac{\text{mJ}}{\text{mol K}^4} \text{ for } \text{SrMn}_2\text{As}_2 \quad (5)$$

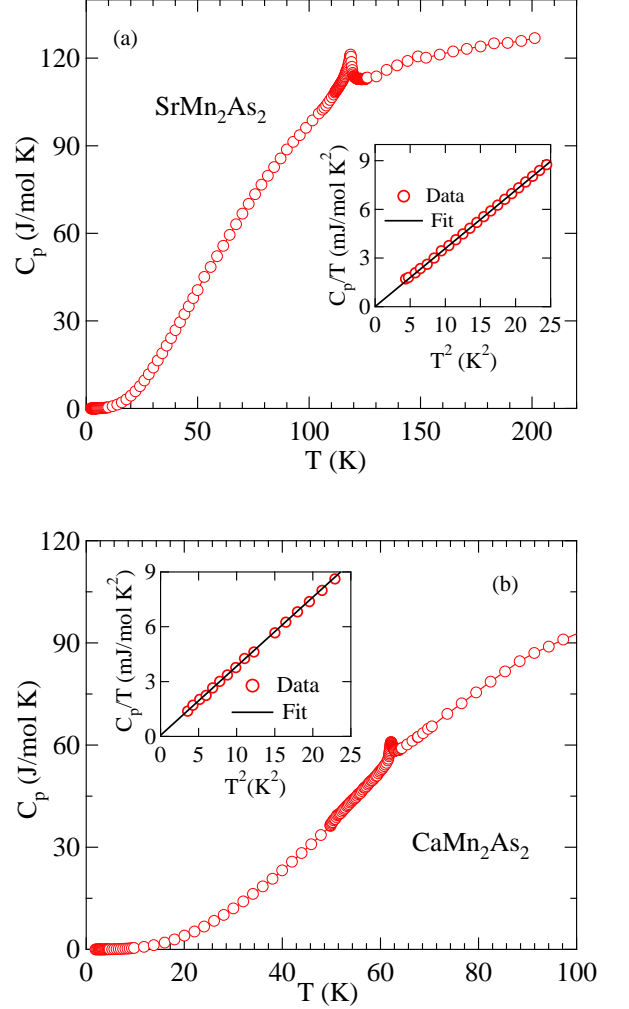


FIG. 8: (Color online) Heat capacity C_p versus temperature T for (a) SrMn_2As_2 and (b) CaMn_2As_2 . The insets show $C_p(T)/T$ versus T^2 for $T < 5$ K, where the straight lines though the respective data are fits by Eq. (4).

and $0.37(1)$ mJ/(mol K⁴) for CaMn_2As_2 . We estimate the Debye temperatures Θ_D for the two compounds from the Debye theory according to⁴⁸

$$\Theta_D = \left(\frac{12\pi^4 R n}{5\beta} \right)^{1/3} \quad (6)$$

where R is the molar gas constant and n is the number of atoms per formula unit [$n = 5$ for SrMn_2As_2 and CaMn_2As_2]. We obtain

$$\Theta_D = 303(3) \text{ K} \quad (\text{SrMn}_2\text{As}_2), \quad (7a)$$

$$= 297(3) \text{ K} \quad (\text{CaMn}_2\text{As}_2). \quad (7b)$$

In the absence of anisotropy gaps in the AFM spin-wave spectrum, contributions to β could arise from excitations

of three-dimensional AFM spin waves at the low temperatures at which the β values were extracted; hence the quoted values of Θ_D are lower limits.

2. Magnetic Contributions to the Heat Capacity and Entropy of SrMn₂As₂

Here we extract estimates of the magnetic contribution $C_{\text{mag}}(T)$ to the measured heat capacity of SrMn₂As₂ and from that we obtain the magnetic contribution $S_{\text{mag}}(T)$ to the entropy over the temperature range from 1.8 to 200 K of the $C_p(T)$ measurements. To accomplish this goal we first obtain an estimate of the lattice contribution $C_{\text{latt}}(T)$ to the measured $C_p(T)$. We use the expression

$$C_{\text{latt}} = nC_{\text{V Debye}}, \quad (8a)$$

where $C_{\text{V Debye}}$ is the Debye lattice heat capacity per mole of atoms given by⁴⁸

$$C_{\text{V Debye}} = 9R \left(\frac{T}{\Theta_D} \right)^3 \int_0^{\Theta_D/T} \frac{x^4 e^x}{(e^x - 1)^2} dx. \quad (8b)$$

The representation of $C_{\text{V Debye}}(T/\Theta_D)$ used here is an accurate analytic Padé approximant function of T/Θ_D obtained by fitting numerical solutions of Eq. (8b) for a list of T/Θ_D values.⁴⁹ The fit of $C_p(T)$ for SrMn₂As₂ in Fig. 9(a) by Eqs. (8) over the temperature range from 1.8 to 60 K and its extrapolation is shown by the blue curve in Fig. 9(a) using the fitted Debye temperature $\Theta_D = 265.7$ K. This value of Θ_D is comparable with the value of 303 K obtained from the fit to the C_p data for SrMn₂As₂ at low T in Eq. (7a), especially considering that Θ_D for a compound typically varies by $\pm 20\%$ on cooling from 300 K to 2 K.⁵⁰

The $C_{\text{mag}}(T)$ is calculated as the difference between the measured $C_p(T)$ and the fitted $C_{\text{latt}}(T)$ in Fig. 9(a). The result is shown in Fig. 9(b), where a sharp peak at $T_N = 120$ K is seen. The C_{mag} at $T > T_N$ shows that there is strong dynamic short-range AFM order above T_N . The magnetic entropy $S_{\text{mag}}(T)$ is calculated from $C_{\text{mag}}(T)$ using

$$S_{\text{mag}}(T) = \int_0^T \frac{C_{\text{mag}}(T)}{T} dT, \quad (9)$$

and the result is shown in Fig. 9(c). The entropy of completely disordered spins S per mole of SrMn₂As₂ and CaMn₂As₂ is $S(T \rightarrow \infty) = 2R \ln(2S + 1)$, which gives

$$S_{\text{mag}}(T \rightarrow \infty) = 23.1 \frac{\text{J}}{\text{mol K}} \quad (S = 3/2) \quad (10a)$$

$$= 29.8 \frac{\text{J}}{\text{mol K}} \quad (S = 5/2), \quad (10b)$$

as shown by the horizontal dashed black lines in Fig. 9(c). This range of spin values encompasses the known variations in the ordered moments of Mn spins in various materials similar to ours which can arise from quantum fluctuation and/or hybridization effects (see, e.g., Ref. 21).

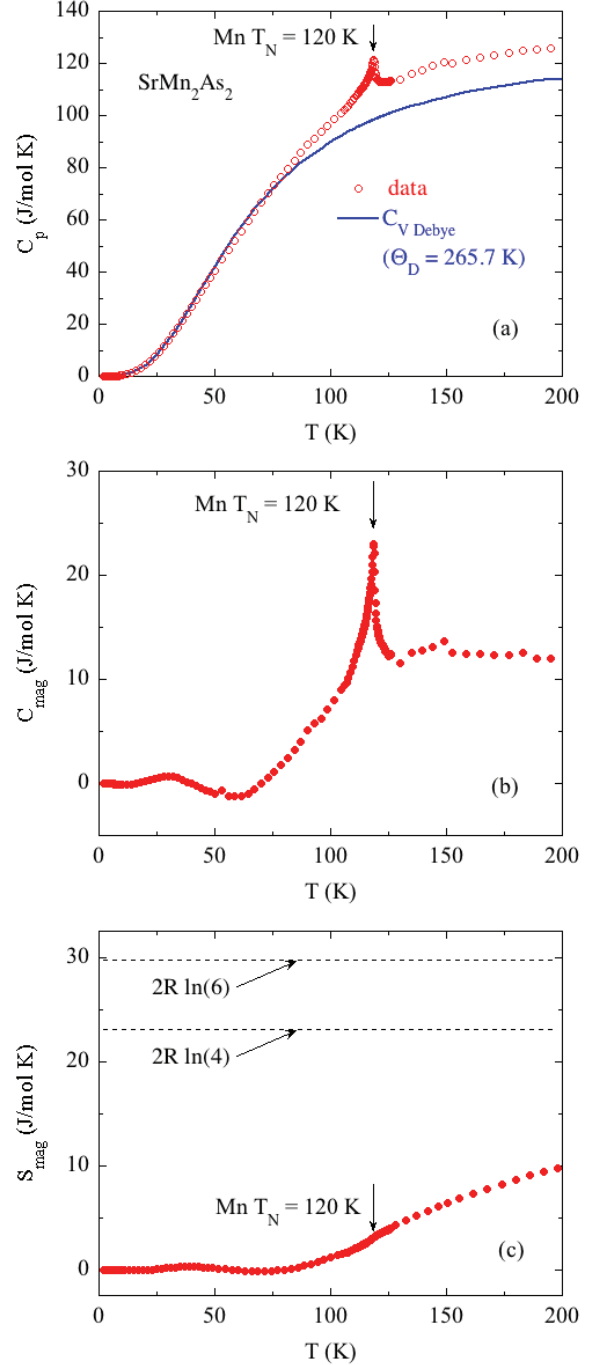


FIG. 9: (Color online) (a) Heat capacity C_p versus T for SrMn₂As₂ and a fit of $C_{\text{V Debye}}(T)$ in Eqs. (8) to the data for $T = 1.8$ K to 60 K. (b) Magnetic heat capacity $C_{\text{mag}}(T)$. (c) Magnetic entropy $S_{\text{mag}}(T)$ obtained using Eq. (9). The dashed lines are $S_{\text{mag}}(T \rightarrow \infty)$ for $S = 5/2$ and $S = 3/2$.

We find that $S_{\text{mag}}(200 \text{ K}) \approx 10 \text{ J/mol K}$ in Fig. 9(c) is only $\approx 33\%$ of the value for $S = 5/2$ in Eqs. (10) and is still only $\approx 43\%$ of the value for $S = 3/2$. Thus the strong short-range AFM order revealed in the $C_{\text{mag}}(T)$ and $S_{\text{mag}}(T)$ data above T_N is consistent with the above conclusion from the $\chi(T)$ data that strong short-range

AFM order survives from T_N up to at least 900 K.

IV. SUMMARY

We have shown that SrMn_2As_2 and CaMn_2As_2 are AFM insulators with Néel temperatures $T_N = 120$ K and 62 K, respectively. The microscopic origin of this large difference in magnitude of the Néel temperatures together with the reason why the Sr compound has a higher T_N than the Ca one, in spite of the smaller unit cell of the latter, remain to be explained.

The $\chi(T)$ data at $T \leq T_N$ indicate that the hexagonal c axis is a hard axis, with the ordered Mn spin-5/2 moments lying within the ab plane. Since a collinear AFM structure within the ab plane is inferred for SrMn_2As_2 from neutron diffraction measurements that were carried out in a companion study,³⁹ the nonzero limits of $\chi_{ab}(T < T_N)$ observed for this compound must arise from the three collinear AFM domains with their axes at 60° to each other within the ab plane. If the populations of the three domains are equal, within molecular field theory one obtains $\chi_{ab}(T \rightarrow 0) = \chi(T_N)/2$, in approximate agreement with the $\chi_{ab}(T)$ data in Fig. 4(a). The prediction of the easy axis arising from the Mn–Mn magnetic dipole interactions in a collinear magnetic structure of SrMn_2As_2 obtained using the formalism of Ref. 45 and the experimental crystal structure is that the ordered moments should lie in the ab plane as inferred here from the

$\chi(T)$ data and also observed³⁹ in the neutron diffraction experiments.

Thus the potential geometric frustration for AFM ordering within the triangular-lattice bilayers parallel to the ab plane that originally motivated this work is apparently not important in SrMn_2As_2 and CaMn_2As_2 . In particular, if AFM Mn–Mn exchange interactions within a triangular sublattice layer were dominant, a non-collinear AFM structure would have resulted instead of the observed³⁹ collinear AFM structure.

Strong dynamic AFM short-range correlations up to at least 900 K as observed in our $\chi(T)$ measurements, consistent with our $S_{\text{mag}}(T)$ data up to 200 K, are likely due to quasi-two-dimensional connectivity of strong AFM Mn–Mn exchange interactions within the corrugated honeycomb Mn layers. This in turn offers the possibility of novel electronic ground states arising upon doping these materials into the metallic state.

Acknowledgments

We thank P. Das, A. Kreyssig and A. I. Goldman for helpful discussions. This research was supported by the U.S. Department of Energy, Office of Basic Energy Sciences, Division of Materials Sciences and Engineering. Ames Laboratory is operated for the U.S. Department of Energy by Iowa State University under Contract No. DE-AC02-07CH11358.

* Present address: Department of Physics and Astronomy, Texas A&M University, College Station, Texas 77840-4242, USA

† Electronic address: johnston@ameslab.gov

¹ G. Just and P. Paufler, J. Alloys Compd. **232**, 1 (1996).

² D. C. Johnston, Adv. Phys. **59**, 803 (2010).

³ G. R. Stewart, Rev. Mod. Phys. **83**, 1589 (2011).

⁴ D. J. Scalapino, Rev. Mod. Phys. **84**, 1383 (2012).

⁵ E. Dagotto, Rev. Mod. Phys. **85**, 849 (1913).

⁶ R. M. Fernandes, A. V. Chubukov, and J. Schmalian, Nat. Phys. **10**, 97 (2014).

⁷ H. Hosono and K. Kuroki, Physica C **514**, 399 (2015).

⁸ P. Dai, Rev. Mod. Phys. **87**, 855 (2015).

⁹ D. S. Inosov, Compt. Rend. Phys. **17**, 60 (2016).

¹⁰ Q. Si, R. Yu, and E. Abrahams, Nat. Rev. Mater. **1**, 1 (2016).

¹¹ E. D. Bauer, F. Ronning, B. L. Scott, and J. D. Thompson, Phys. Rev. B **78**, 172504 (2008).

¹² F. Ronning, N. Kurita, E. D. Bauer, B. L. Scott, T. Park, T. Klimczuk, R. Movshovich, and J. D. Thompson, J. Phys.: Condens. Matter **20**, 342203 (2008).

¹³ A. Pandey, D. G. Quirinale, W. Jayasekara, A. Sapkota, M. G. Kim, R. S. Dhaka, Y. Lee, T. W. Heitmann, P. W. Stephens, V. Ogloblichev, A. Kreyssig, R. J. McQueeney, A. I. Goldman, A. Kaminski, B. N. Harmon, Y. Furukawa, and D. C. Johnston, Phys. Rev. B **88**, 014526 (2013).

¹⁴ W. Jayasekara, Y. Lee, A. Pandey, G. S. Tucker, A.

Sapkota, J. Lamsal, S. Calder, D. L. Abernathy, J. L. Niedziela, B. N. Harmon, A. Kreyssig, D. Vaknin, D. C. Johnston, A. I. Goldman, and R. J. McQueeney, Phys. Rev. Lett. **111**, 157001 (2013).

¹⁵ P. Wiecki, V. Ogloblichev, A. Pandey, D. C. Johnston, and Y. Furukawa, Phys. Rev. B **91**, 220406(R) (2015).

¹⁶ A. S. Sefat, D. J. Singh, R. Jin, M. A. McGuire, B. C. Sales, and D. Mandrus, Phys. Rev. B **79**, 024512 (2009).

¹⁷ V. K. Anand, D. G. Quirinale, Y. Lee, B. N. Harmon, Y. Furukawa, V. V. Ogloblichev, A. Huq, D. L. Abernathy, P. W. Stephens, R. J. McQueeney, A. Kreyssig, A. I. Goldman, and D. C. Johnston, Phys. Rev. B **90**, 064517 (2014).

¹⁸ P. Wiecki, B. Roy, D. C. Johnston, S. L. Bud'ko, P. C. Canfield, and Y. Furukawa, Phys. Rev. Lett. **115**, 137001 (2015).

¹⁹ Y. Singh, A. Ellern, and D. C. Johnston, Phys. Rev. B **79**, 094519 (2009).

²⁰ Y. Singh, M. A. Green, Q. Huang, A. Kreyssig, R. J. McQueeney, D. C. Johnston, and A. I. Goldman, Phys. Rev. B **80**, 100403(R) (2009).

²¹ D. C. Johnston, R. J. McQueeney, B. Lake, A. Honecker, M. E. Zhitomirsky, R. Nath, Y. Furukawa, V. P. Antropov, and Y. Singh, Phys. Rev. B **84**, 094445 (2011).

²² A. Antal, T. Knoblauch, Y. Singh, P. Gegenwart, D. Wu, and M. Dressel, Phys. Rev. B **86**, 014506 (2012).

²³ S. Calder, B. Saparov, H. B. Cao, J. L. Niedziela, M. D. Lumsden, A. S. Sefat, and A. D. Christianson, Phys. Rev.

- B **89**, 064417 (2014).
- ²⁴ A. Pandey, R. S. Dhaka, J. Lamsal, Y. Lee, V. K. Anand, A. Kreyssig, T. W. Heitmann, R. J. McQueeney, A. I. Goldman, B. N. Harmon, A. Kaminski, and D. C. Johnston, Phys. Rev. Lett. **108**, 087005 (2012).
 - ²⁵ S. Yeninas, A. Pandey, V. Ogloblichev, K. Mikhalev, D. C. Johnston, and Y. Furukawa, Phys. Rev. B **88**, 241111(R) (2013).
 - ²⁶ J.-K. Bao, H. Jiang, Y.-L. Sun, W.-H. Jiao, C.-Y. Shen, H.-J. Guo, Y. Chen, C.-M. Feng, H.-Q. Yuan, Z.-A. Xu, G.-H. Cao, R. Sasaki, T. Tanaka, K. Matsubayashi, and Y. Uwatoko, Phys. Rev. B **85**, 144523 (2012).
 - ²⁷ A. Pandey, B. G. Ueland, S. Yeninas, A. Kreyssig, A. Sapkota, Yang Zhao, J. S. Helton, J.W. Lynn, R. J. McQueeney, Y. Furukawa, A. I. Goldman, and D. C. Johnston, Phys. Rev. Lett. **111**, 047001 (2013).
 - ²⁸ B. G. Ueland, A. Pandey, Y. Lee, A. Sapkota, Y. Choi, D. Haskel, R. A. Rosenberg, J. C. Lang, B. N. Harmon, D. C. Johnston, A. Kreyssig, and A. I. Goldman, Phys. Rev. Lett. **114**, 217001 (2015).
 - ²⁹ A. Pandey and D. C. Johnston, Phys. Rev. B **92**, 174401 (2015).
 - ³⁰ J. Lamsal, G. S. Tucker, T. W. Heitmann, A. Kreyssig, A. Jesche, A. Pandey, W. Tian, R. J. McQueeney, D. C. Johnston, and A. I. Goldman, Phys. Rev. B **87**, 144418 (2013).
 - ³¹ A. Mewis, Z. Naturforsch. **33b**, 606 (1978).
 - ³² E. Brechtel, G. Cordier, and H. Schäfer, Z. Naturforsch. **33b**, 820 (1978).
 - ³³ A. P. Ramirez, Annu. Rev. Mater. Sci. **24**, 453 (1994).
 - ³⁴ R. Moessner and A. P. Ramirez, Physics Today **59**, 24 (2006).
 - ³⁵ L. Balents, Nature **464**, 199 (2010).
 - ³⁶ Z.W. Wang, H.X. Yang, H.F. Tian, H.L. Shi, J.B. Lu, Y.B. Qin, Z. Wang, J.Q. Li, J. Phys. Chem. Solids **72**, 457 (2011).
 - ³⁷ W. Ratcliff II, A. L. Lima Sharma, A. M. Gomes, J. L. Gonzalez, Q. Huang, and J. Singleton, J. Magn. Magn. Mater. **321**, 2612 (2009).
 - ³⁸ C. A. Bridges, V. V. Krishnamurthy, S. Poulton, M. P. Paranthaman, B. C. Sales, C. Myers, and S. Bobev, J. Magn. Magn. Mater. **321**, 2653 (2009).
 - ³⁹ P. Das, N. S. Sangeetha, A. Pandey, Z. A. Benson, T. W. Heitmann, D. C. Johnston, A. I. Goldman, and A. Kreyssig, arXiv:1605.02004.
 - ⁴⁰ J. Rodríguez-Carvajal, Phys. B: Condens. Matter **192**, 55 (1993).
 - ⁴¹ D. C. Johnston, Phys. Rev. Lett. **109**, 077201 (2012).
 - ⁴² D. C. Johnston, Phys. Rev. B **91**, 064427 (2015).
 - ⁴³ V. K. Anand and D. C. Johnston, Phys. Rev. B **91**, 184403 (2015).
 - ⁴⁴ D. H. Ryan, J. M. Cadogan, V. K. Anand, D. C. Johnston, and R. Flacau, J. Phys.: Condens. Matter **27**, 206002 (2015).
 - ⁴⁵ D. C. Johnston, Phys. Rev. B **93**, 014421 (2016).
 - ⁴⁶ S. Haneda, N. Kazama, Y. Yamaguchi, and H. Watanabe, J. Phys. Soc. Jpn. **42**, 1201 (1977).
 - ⁴⁷ B. Saparov, J. E. Mitchell, and A. S. Sefat, Supercond. Sci. Technol. **25**, 084016 (2012).
 - ⁴⁸ C. Kittel, *Introduction to Solid State Physics* (Wiley, Hoboken, NJ, 2005).
 - ⁴⁹ R. J. Goetsch, V. K. Anand, A. Pandey, and D. C. Johnston, Phys. Rev. B **85**, 054517 (2012).
 - ⁵⁰ J. S. Smart, *Effective Field Theories of Magnetism* (Saunders, Philadelphia, 1966).